Solid-immersion imaging interferometric nanoscopy to the limits of available frequency space

Yuliya Kuznetsova, Alexander Neumann, and S. R. J. Brueck*

*Center for High Technology Materials and Departments of Electrical and Computer Engineering and Physics
and Astronomy, University of New Mexico, Albuquerque, New Mexico 87106, USA*
Corresponding author: brueck@chtm.unm.edu

Imaging interferometric nanoscopy (IIN) is a synthetic aperture approach offering the potential of optical resolution to the linear-system limit of optics ($\sim\lambda/4n$). The immersion advantages of IIN can be realized if the object is in close proximity to a solid-immersion medium with illumination and collection through the substrate and coupling this radiation to air by a grating on the medium surface opposite the object. The spatial resolution as a function of the medium thickness and refractive index as well as the field-of-view of the objective optical system is derived and applied to simulations.   © 2012 Optical Society of America

OCIS codes: 180.0180, 110.0110.

1. INTRODUCTION

Microscopy is among the most important scientific and technological uses of optics. The diffraction limits to optical resolution were established over a century ago; the maximum spatial frequency allowed by an optical system is $2NA/\lambda$ [1], giving a resolution [half-pitch (HP)] limit of $\lambda/4NA$, where λ is the optical wavelength and NA is the numerical aperture of the optical system. The quest for optical superresolution has long been a topic of great scientific and practical interest [2–36]. For the case of fluorescence imaging, numerous nonlinear techniques have been introduced that have demonstrated resolution to $\sim$10 nm, well below the diffraction limit [37]. Hyperlenses, based on nonplanar, layered material structures have demonstrated resolution to $\sim\lambda/3$, albeit with a subwavelength field of view (FOV) [38,39]. Among the techniques for structural (sensitive to refractive index variations) microscopy, imaging interferometric nanoscopy (IIN) is an attractive alternative that takes advantage of synthetic apertures, using multiple illumination and collection directions, to obtain a series of subimages, which are then numerically reconstructed into a full image [40–43]. A significant advantage of IIN is that the FOV, working distance, and depth of field of the original imaging system are retained. Resolution has been demonstrated to the linear-system limits in air [40–42], $\lambda/4$, independent of the lens NA.

Immersion techniques to further extend resolution are well known. Traditional oil-immersion microscopy uses lenses of NA $\sim 1.3 - 1.4$, and it has recently been extended with off-axis illumination techniques [44]. Solid-immersion microscopy can achieve even higher resolutions, with NA ~ 3.5 for application to circuits on a silicon substrate [45]. Similarly, IIN can be extended by solid-immersion techniques, whereby a slab of material with a high index of refraction is used as a solid-immersion medium. A major advantage for many applications is that IIN can use very thin immersion slabs (down to fractions of a wavelength), which makes the use of highly absorbing materials feasible. In such cases, the wavelength can be

chosen shorter than the bandgap of the immersion material to take advantage of the increasing refractive index within an absorption band; both the shorter wavelength and the larger index extend the resolution well beyond that available with any other known linear system microscopy strategy, even within the same $\lambda/4n$ linear-system frequency-space limit, where n is the immersion material refractive index.

There are several ways to adapt IIN for solid immersion. A high-index slab can be placed very close to the object (within range of the evanescent fields). The slab can be a multilayer structure or a confined liquid. For the present treatment, we consider a substrate, transparent at the IIN wavelength, as the immersion slab. Recently, we demonstrated a resolution $<\lambda/5$ for IIN of high contrast, chrome-on-glass objects on a glass substrate by illumination through the evanescent fields of the substrate and conventional collection in air (including off-axis contributions) [46]. For compactness, this configuration is referred to below as half-immersion (e.g., the illumination takes advantage of the higher wave vectors in the substrate, but the collection is limited to scattered wave vectors that propagate in air). For this configuration, the limiting optical resolution, in the Abbe sense of the smallest available HP in the optical response, is $\lambda/[2(n + 1)]$.

Clearly, the resolution can be further extended by collection of the reflected backscattered light that propagates in the substrate beyond the angle for total internal reflection. This scattering corresponds to larger wavenumbers and therefore to information on smaller details of the sample. We introduce a grating on the back side of the substrate to extract this scattered information, making it accessible to the optical collection system. There are spatial-frequency-dependent distortions associated with the spreading of the information as it propagates across the substrate and extends spatially beyond the FOV of the collection system and phase aberrations associated this extended propagation, which require an algorithm for transforming the image from the laboratory frame to the image frame for combination with other subimages. The

linear-system limit is a resolution of $\lambda/4n$; resolution very close to this limit can be achieved in many cases, however, with interrelated requirements on the FOV, the NA, and the thickness and refractive index of the substrate. The aims of this work are as follows: to quantify the relationship between these parameters and the number of required subimages and to elucidate the transformation procedure for subimages for deep subwavelength cases with full immersion, including single and multiple backside subimages. We make a distinction between techniques that use a grating in the plane of the object [9] (often to extract near-field information [35]) and our technique, which uses a grating displaced from the object by the thickness of the substrate to extract propagating waves in the substrate beyond the angle for total internal reflection and make them available for collection in free space.

The original (nonimmersion) IIN optical arrangement is shown schematically in Fig. 1. The result is the capture of a subimage consisting of a separate region of frequency space in each subimage. In air, the maximum angle of illumination can approach $90°$, but it is of course smaller in the substrate as a result of refraction at the air–substrate interface. By coupling into internal modes of the substrate, grazing incidence in the substrate can be achieved, increasing the resolution [46]. IIN relies on recording and combining subimages to produce a final image that covers all of the essential, object dependent, parts of frequency space.

Using only a modest NA = 0.4 lens at $\lambda = 633$ nm and an object supported on a substrate with refractive index n, we have demonstrated a half-immersion imaging resolution with evanescent wave illumination to a maximum spatial frequency of $(n + \text{NA})/\lambda$ with the objective normal to the substrate (e.g., untilted objective; 170 nm features on a glass substrate with $n = 1.5$) and up to $(n + 1)/\lambda$ with a tilted objective (150 nm features of arbitrary structures, while the theoretical limit of grating HP resolution is 126 nm) [46]. We note in passing that tilting the objective lens, and correcting for the nonparaxial distortions this introduces, is a cumbersome operation. We will look for approaches to make it easier to collect the spatial frequency information between $(n + \text{NA})/\lambda$ and $(n + 1)/\lambda$ as well as extending the spatial frequency coverage towards $2n/\lambda$ by adding a grating coupler on the side of the substrate opposite the object. Phase and intensity matching of the subimages is achieved electronically using a reference object containing spatial frequencies within each recorded subimage.

The illumination and collection configurations for half-immersion and full-immersion are shown in Fig. 2a). The illumination laser beam is coupled into the substrate (using a prism, a grating, or end fire coupling), and the object is illuminated by an evanescent wave. Image frequencies up to $(n + \text{NA})/\lambda$ can be captured with an objective normal to the sub-

strate surface [Fig. 2a), objective A], and frequencies up to $(n + 1)/\lambda$ with tilt of the objective off of the optic axis [Fig. 2a), objective B]. The evanescent waves from the higher frequency content of the object are coupled back into the substrate by the boundary conditions at the substrate interface, and for spatial frequencies between $(n + 1)/\lambda$ and $2n/\lambda$ propagate in the substrate at angles beyond the angle for total internal reflection. For a flat interface, the information at these spatial frequencies is not accessible, but the scattered light can be decoupled by a grating on the side of the substrate opposite to the object and redirected to an objective on the grating side, opposite the sample [Fig. 2a), objective C]. This optical system (the required coherent reference beam is not shown) leads to frequency aliasing as a result of the grating diffraction. While this can be corrected with the reference beam, it is usually preferable to offset the subimage spatial frequencies to lower intermediate frequencies to reduce the pixel size and density requirement at the collection system focal plane and restore the actual frequencies computationally before combining subimages. In addition, there are phase errors (aberrations) associated with the collection system which includes partial propagation both in the high-index substrate and in air. The treatment of these spatial frequency and phase corrections is discussed below.

The corresponding frequency-space coverages are shown in Fig. 2b). Normal incidence illumination and collection from the sample side is the traditional coherent illumination configuration represented by the small red circle with frequency-space coverage to NA/λ. Illumination at an angle of $2\text{NA}/\lambda$ provides the offset orange circles with frequency-space coverage to $3\text{NA}/\lambda$. For a Manhattan geometry object, two subimages providing coverage in the x, y directions is typically used, additional subimages, indicated by the lighter orange circles (at $45°$ to the principal x, y axes) can be added for additional off-grid frequency-space coverage. The illumination and sample-side collection scheme of Fig. 2a) allow increasing the spatial frequency coverage to $(n + \text{NA})/\lambda$ (green circles). Collection with a tilted objective allows frequency-space coverage to $(n + 1)/\lambda$. Finally, the substrate-side collection discussed in this contribution extends the frequency-space coverage to the linear-system limit of $2n/\lambda$ with a corresponding Abbe HP of $\lambda/4n$.

IIN requires reintroducing a coherent zero-order reference at the image plane (e.g., constructing an interferometer around the objective lens) to record the amplitude and phase of the spectral frequencies in the subimages. As has been discussed in previous papers [41,43], the intensity, angle and phase of the reference beam have to be chosen to match all subimages to the on-axis image. For this purpose we use a reference object covering a small part of the FOV in
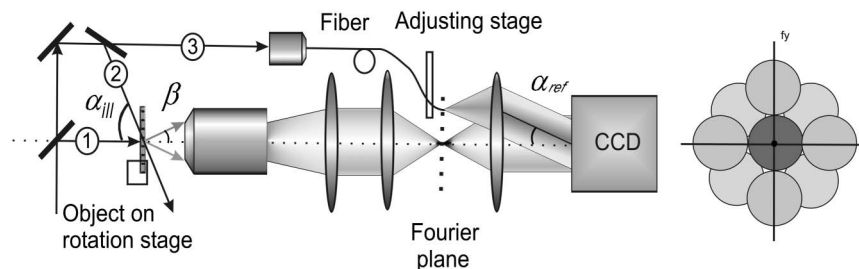

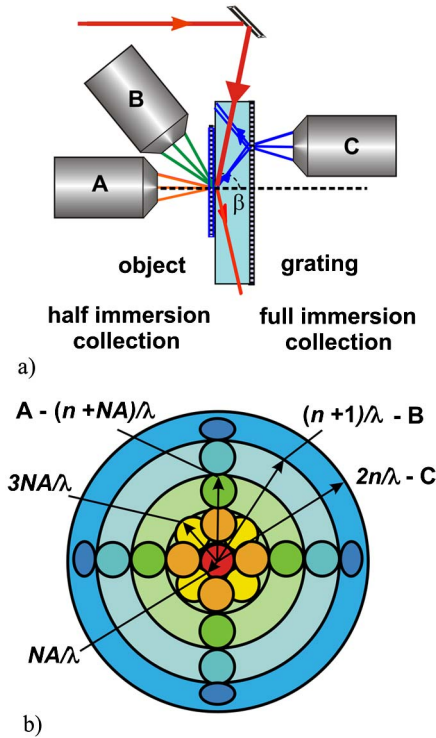Fig. 1. IIN optical arrangement (described in detail in [41]).

Fig. 2. (Color online) a) Illumination and collection configurations: A—objective normal to the substrate surface, image frequencies up to $(n + \text{NA})/\lambda$ can be captured; B—objective with tilt away from the optic axis, frequencies up to $(n + 1)/\lambda$; C—objective on the side of the substrate with grating, frequencies between $(n + 1)/\lambda$ and $2n/\lambda$. b) spatial frequency-space coverage with regions collected with various geometries indicated.

order to determine the correct intensity ratio, frequency shift, and phase. These offset frequencies are then corrected in the image processing before the subimages are combined.

One more preamble is necessary before tackling the image reconstruction. The description that follows has elements of ray tracing (looking at the propagation of scattered rays corresponding to specific spatial frequencies) and of Fourier optics (based on "infinite" plane wave propagation). The solution to this duality is to consider "wave packets" with center spatial frequencies that correspond to the direction of propagation and with a spatial extent that corresponds to the FOV, which is assumed to be much larger than the individual scattering objects within the field, but much smaller than the diameter of the lens. This of course corresponds to a broadening in the pupil plane and Fourier planes from the delta functions associated with plane waves to diffraction patterns corresponding to the finite FOV.

2. FULL-IMMERSION FREQUENCY-SPACE COVERAGE

The goal of this investigation is to explore the collection of additional scattered information at spatial frequencies beyond $(n + \text{NA})/\lambda$ by collection from the back side of the substrate using one or more gratings to redirect this information into an objective lens. The model presented here is based on a Fourier decomposition of the scattered (reflected) image along with geometrical analysis of the diffraction path for each component. It is clear from the geometry of Fig. 3 that the spatial frequency coverage of each subimage depends on the thick-

ness and refractive index of the substrate as well as on the FOV and NA of the objective lens. For thicker substrates, the relevant information is spread across a wider area requiring a larger FOV. This may require multiple spatially displaced subimages to extract all of the information (a synthetic FOV). If the available information extends beyond the $2\text{NA}/\lambda$ bandwidth of the collection optics, multiple gratings are required (a synthetic aperture). The minimum collected spatial frequency (angle α_1 in Fig. 3) sets the period d of the extraction grating:

$$d = \frac{\lambda}{n \sin \alpha_1 + \text{NA}}. \tag{1}$$

If this frequency equals the maximum available from half-immersion without a tilted objective, $(n + \text{NA})/\lambda$, then

$$d = \frac{\lambda}{2\text{NA}}. \tag{2}$$

This takes a scattered wave in the substrate corresponding to

$$k_{\alpha_1} = k_0 \text{NA} = n k_0 \sin \alpha_1 = n k_0 \sin\left[\sin^{-1}(\text{NA}/n)\right] \tag{3}$$

into a wave propagating in air at an angle $-\sin^{-1}(\text{NA})$. Here, $k_0 \equiv 2\pi/\lambda$. Note that provided $\text{NA} > 0.33$, higher diffraction orders from the grating are outside the NA of the collection optics and do not interfere with the image; we consider an $\text{NA} = 0.4$ in the modeling. Over the range of spatial frequencies collected in each subimage, the diffraction efficiencies are roughly constant, thus allowing intensity compensation by subimage matching procedures [41–43]. This arrangement is free of the complications connected with multiple diffraction orders from gratings in comparison to the methods proposed by Lukosz [9] and Sentenac *et al.* [35]. In our case, the gratings provide extraction of information out of the immersion media but not diffraction of near-field high-spatial frequency components directly from the object. There can be variations in diffraction efficiency as the various higher order beams, in both the substrate and in air, switch from evanescent to propagating waves. These are easily dealt with empirically by adjusting the amplitudes of the relevant portions of each subimage independently, either by physically restricting the collection NA appropriately, or by separately addressing the regions of the subimage electronically.

Progressively higher spatial frequency components impinge on the grating at larger horizontal displacements from the object and are diffracted into increasing angles, until the scattered beam at a displacement of $b + F$ from the object centerline is diffracted at to an angle of $+\theta$ in air. The distance
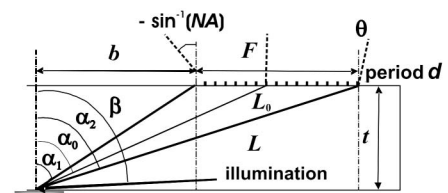

Fig. 3. Geometry shows the collection of high-spatial-frequency information propagating in the substrate that corresponds to small features.

F corresponds to the FOV of the objective lens, which we take as focused on the grating surface, or to the width of the grating if it is smaller than the FOV. Provided $\theta \le \sin^{-1}(\text{NA})$, the entire spread of scattered light incident on the grating is collected by the objective lens. From the geometry of Fig. 3, several important relationships are readily derived:

$$\sin(\alpha_1) = \frac{\text{NA}}{n} = \frac{b}{\sqrt{b^2 + t^2}}; \qquad b = t\left[\left(\frac{n}{\text{NA}}\right)^2 - 1\right]^{-1/2}, \quad (4)$$

$$\sin(\alpha_2) = \frac{b + F}{\sqrt{(b+F)^2 + t^2}} = \left[1 + \left(\frac{b+F}{t}\right)^{-2}\right]^{-1/2},$$

$$= \left\{1 + \left[\frac{F}{t} + \left(\left(\frac{n}{\text{NA}}\right)^2 - 1\right)^{-1/2}\right]^{-2}\right\}^{-1/2} \quad (5)$$

and the corresponding minimum HP is

$$\text{HP}_{\min} = \text{MAX}\left\{\frac{\frac{\lambda}{2(n+3\text{NA})};}{2n\left\{1 + \left\{1 + \left[\frac{F}{t} + \left(\left(\frac{n}{\text{NA}}\right)^2 - 1\right)^{-1/2}\right]^{-2}\right\}^{-1/2}\right\}}\right\}. \quad (6)$$

The upper expression is valid when the full NA of the objective lens is filled by the diffracted beams from the grating; e.g., the grating width F, and the optical FOV and NA are such that $\theta \ge \sin^{-1}(\text{NA})$. If the angular spread is restricted by the FOV, or equivalently by the width of the grating, the lower expression pertains. An additional constraint is that $3\text{NA} < n$, because only spatial frequencies that can propagate in the substrate can be collected. The limiting behavior of $\text{HP}_{\min}$ is readily evaluated from this expression. For small NA where the full angular width of the lens is filled, the upper expression applies. For all cases of interest, $\text{NA}/n \ll 1$; that is, the lens NA is much less than the refractive index of the immersion medium. For large fields of view or thin substrates, $F/t \gg \text{NA}/n$, $\text{HP}_{\min} \to \lambda/[n(4 - (t/F)^2)]$. Thus, $\text{HP}_{\min}$ is always larger than the optics linear-system limit. The upper limit in Eq. (6) takes over before this result; thus, the NA of the lens is filled in just a single subimage. Additional gratings at smaller pitches of $\lambda/2(i+1)\text{NA}$ $[i = 1, 2, 3, \ldots]$ allow access to higher spatial frequency components of the image up to the linear-system limit of $\lambda/4n$. In the opposite limit, $\text{NA}/n \ll 1$ and $F/t \ll \text{NA}/n$, $\text{HP}_{\min} \to \lambda/[2(n + \text{NA} + \frac{nF}{t})]$. The resolution is always somewhat improved over the starting point of half-immersion with the collection system optical axis normal to the object plane. In this case, the linear-system limit of $\lambda/4n$ can be approached with a synthetic FOV, e.g., multiple subimages with the collection optical system displaced to collect the higher spatial frequencies that are lost by the limited FOV with the same grating (synthetic FOV), and again, with multiple gratings (synthetic aperture), it is possible to extend the resolution close to the $\lambda/4n$ limit, as long as signal-to-noise ratio (S/N) is sufficient to enable subimage reconstruction into a full image.

Resolution (HP) restrictions as a function of substrate refractive index for NA = 0.4, 0.8, 1.2, fixed FOV ($F = 32$ μm) and substrate thickness ($t = 50$ μm) obtained from Eq. (6) are shown in Fig. 4. There is a point of transition on each curve (solid to dotted). The solid lines correspond to the upper
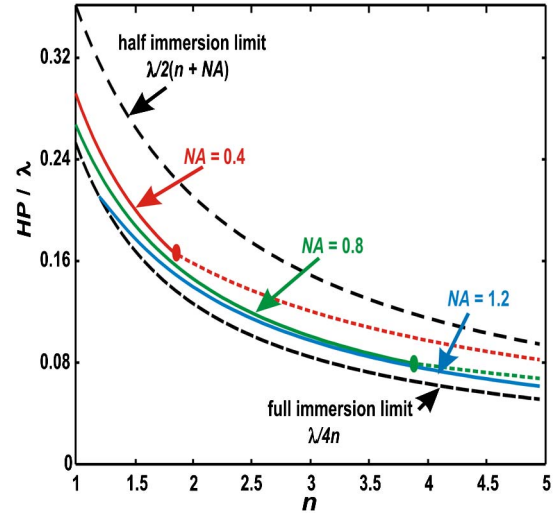

Fig. 4. (Color online) Resolution restriction: normalized HP versus index of refraction for different NAs (0.4, 0.8, 1.2) with a fixed substrate thickness ($t = 50$ μm) and FOV ($F = 32$ μm). Solid lines, dependence described by the lower part of Eq. (6); dashed lines, dependence described by the upper part of Eq. (6).

expression of Eq. (6); the dotted lines to the lower form. In the dotted region, additional subimages are required to synthesize a larger FOV. Once the lens NA is filled, an additional grating is required to extract higher spatial frequency information and alias it into the lens NA, e.g., to synthesize a larger NA.

The combination of restrictions induced by substrate properties and synthetic aperture (multiple of NA = 0.4) for a fixed FOV ($F = 32$ μm) with varying substrate thickness are shown in Fig. 5. The curves correspond to substrate thicknesses of 10, 30, 100, and 300 μm with break points denoted by the transitions from dashed to dotted lines by curves of synthetic NA restrictions. Here, $\lambda/[2(n + 3\text{NA})]$ corresponds
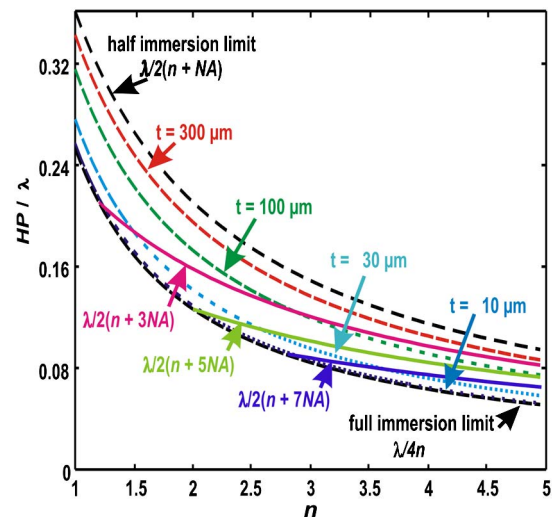

Fig. 5. (Color online) Resolution restriction: normalized HP versus index of refraction for different substrate thicknesses: 10–, 30–, 100–, 300 μm calculated with NA = 0.4, $F = 32$ μm in different synthetic aperture steps: long dashed lines, inside of synthetic aperture up to $\lambda/[2(n + 3\text{NA})]$; dashed lines, inside of synthetic aperture up to $\lambda/[2(n + 5\text{NA})]$; dotted lines, inside of synthetic aperture up to $\lambda/[2(n + 7\text{NA})]$.

to upper part of Eq. ([6](#)). The restrictions $\lambda/[2(n + 5NA)]$ and $\lambda/[2(n + 7NA)]$ appear by synthetic aperture extension with one and two additional aperture intervals along each spatial direction using adapted gratings for each interval, as described above.

We can infer from Figs. [4](#) and [5](#) that, for a single subimage, a small-NA optical system can give useful resolution extensions only for materials with a low index of refraction. In order to reach high resolution using materials with high n, we need either additional subimages using multiple gratings or an objective with higher NA. A larger FOV objective enhances the resolution but typically is associated with lower NA, which again requires additional subimages. A compromise between FOV and NA has to be found for the chosen substrate thickness and index of refraction to minimize the total number of subimages. These models do not include the impact of a finite S/N. As the signal becomes more dispersed with thicker substrates, the S/N decreases and stochastic (noise) contributions to the image become more significant, limiting the ability to accurately combine the subimages and construct a composite image.

3. FULL-IMMERSION IMAGE RECONSTRUCTION

An initial experiment, the only experimental result presented, was conducted using a 1 mm thick glass substrate optically coupled to a second 1 mm thick microscope slide with a metal decoupling grating of period 560 nm. Thus the total thickness (object to grating) is 2 mm. The results showed the possibility of resolution of periodic structures at scales beyond the previously demonstrated half-immersion limit. The image consists of a repeated pattern of several parallel lines with a spacing of 240 nm within a trapezoidal envelope. The pattern is repeated at a spacing of 3.6 μm in both directions. A SEM image is shown in Fig. [6a)](#). The x-direction high-frequency image was recorded and is shown in Fig. [6b)](#). The high-frequency image contains much of the information about the original pat-
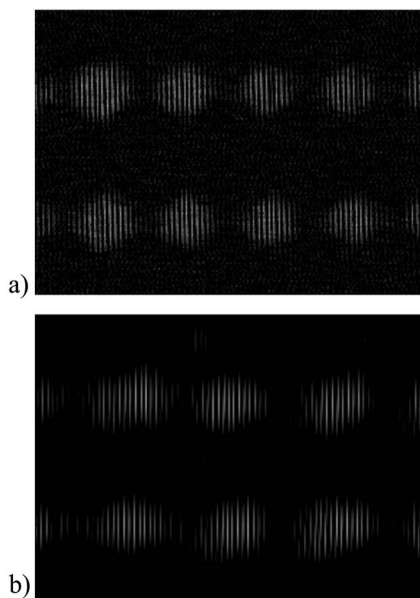

a)

b)

Fig. 6.   a) SEM image of periodic structure, HP = 120 nm and b) IIN subimage for $t = 2$ mm and decoupling grating HP of 280 nm.

a)

b)

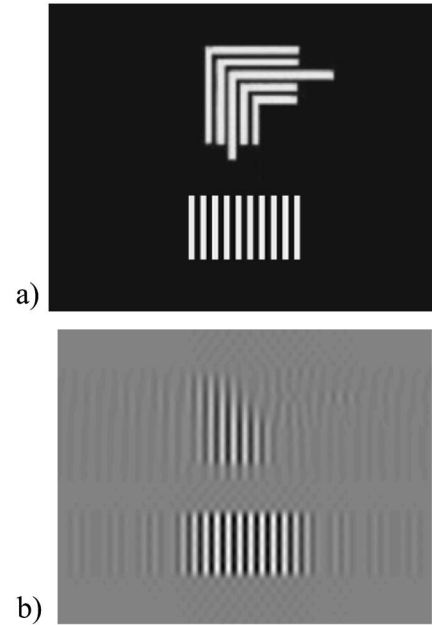Fig. 7.   a) Model CD = 120 nm structures, b) x-direction high-frequency image.

tern: the repeated pattern is evident as is the clustering of lines in each repeat unit. However, the image is distorted due to the geometry of propagation in the substrate [Fig. [2b)](#)] and requires a restoration procedure before the proper image can be recovered. Clearly there are fewer clusters at the same transverse scale (3 versus 4) in the distorted image, the relative spacing between the line clusters is changed and there are additional lines in the clusters, though the line pitch remains the same.

This distortion of the image is a result of the propagation in the substrate and depends on the optical path in the substrate, e.g., on the substrate refractive index and thickness. The optical configuration was shown in Fig. [2](#), with the collection lens focused onto the grating surface. Because a diffraction-limited, aberration-free optical system has no phase error between conjugate planes, e.g., the grating surface and the camera focal plane, the only phase variations we need to consider are for propagation in the substrate (Fig. [3](#)). For analytical simplicity, we consider a one-dimensional case; the calculations are readily extended to two-dimensional objects. Let L and L_0 be optical paths of an arbitrary and of the central ray in the substrate, α and α_0 are the angles of the corresponding rays to the substrate normal. θ is the angle of the arbitrary ray to the optical axis after diffraction from the grating and exiting the substrate (the ray must be captured by the objective in air and for convenience is shown as a marginal ray).

The angle α_0 of the ray in the substrate which is redirected along the optical axis in air is

$$\sin \alpha_0 = \frac{\lambda}{nd} = \frac{2NA}{n}. \qquad (7)$$

The marginal ray inclined at the angle α_2 to the normal in the substrate and an angle θ in air after scattering by the grating is described by

$$\sin \alpha_2 = \frac{1}{n}\left(\frac{\lambda}{d} + \sin \theta\right). \tag{8}$$

Then the path lengths in the substrate are

$$L_0 = \frac{t}{\cos \alpha_0} = \frac{t}{\sqrt{1 - \sin^2 \alpha_0}} = \frac{t}{\sqrt{1 - \left(\frac{\lambda}{nd}\right)^2}}, \tag{9}$$

$$L = \frac{t}{\cos \alpha_2} = \frac{t}{\sqrt{1 - \sin^2 \alpha_2}} = \frac{t}{\sqrt{1 - \left[\frac{1}{n}\left(\frac{\lambda}{d} + \sin \theta\right)\right]}}, \tag{10}$$

and the phase difference between the arbitrary ray and the central ray is

$$\Delta\varphi = \varphi - \varphi_0 = \frac{2\pi n t}{\lambda}\left[\frac{1}{\sqrt{1 - \left[\frac{1}{n}\left(\frac{\lambda}{d} + \sin \theta\right)\right]^2}} - \frac{1}{\sqrt{1 - \left(\frac{\lambda}{nd}\right)^2}}\right]. \tag{11}$$

The rays in Fig. 3 are k-vectors of the plane waves propagating at angles θ corresponding to the image spatial frequencies f_x. So, the phases at each spatial frequency can be corrected in Fourier space using the distortion phase function provided by the 2D generalization of Eq. (11). Clearly that distortion phase function [Eq. (11)] provides only a relative phase correction. The constant term (the phase shift introduced by the central ray optical path) will be automatically corrected later by the subimage phase-matching procedure required in IIN, because this constant term is indistinguishable from the arbitrary constant term introduced by the phase of the reference arm of the Mach–Zehnder interferometer inherent in IIN.

Simulation of the impact of this phase distortion on the image with nested-L structure and a delimited grating with CD = 120 nm (Fig. 7) is shown in Fig. 8. The high-spatial-frequency (between NA/λ and 3NA/λ) filtered image of the model is shown in Fig. 7b). The image is expanded; e.g., additional features appear on both sides of object due to lack of compensation in these regions as a result of the optical bandwidth limit. This is just the familiar Gibbs effect associated with an abrupt

cut-off in frequency space. The high-frequency image after the application of the phase aberrations for a substrate thickness of 1 μm [5 μm] is shown in Fig. 8a) [Fig. 8b)] {crosscut Fig. 8c) [Fig. 8d)]}. There is additional walk-off of the intensity versus position as a result of the spreading of the image intensity. The reason for this spread is the progressive walk-off of higher spatial frequency components (phase distortions) as they propagate across the substrate. Here, the additional features appear nonsymmetrically to the illumination side. Also, unlike the Gibbs effect, no information is lost. The step from Fig. 7b) to Figs. 8a), 8b) is completely deterministic and is easily inverted by taking the Fourier transform of the laboratory frame image, applying the inverse of Eq. (11) and retransforming back to the image frame providing all information is captured and there are no S/N limitations. The spatial extent of the image spectrum expands with increasing substrate thickness [compare Figs. 8a) and 8b)]. The intensity spread extension beyond the objective FOV leads to the loss of information which results in reduction of the image quality after restoration. This information can be accessed with a synthetic FOV, e.g., shifting the objective lens to acquire additional subimages with an extended grating at the same pitch.

Without shifting the objective lens, the loss of information is equivalent to the reduction of captured range of frequencies (NA$_{\text{sub}}$ < NA) for a single subimage, which is a function of the FOV. To evaluate this degradation of the image bandwidth in a single image, consider again Fig. 3, but now in a configuration where the grating is chosen so that a particular HP$_c$ is along the optical axis; e.g., fix the optical axis (center) frequency rather than the low-frequency marginal ray. The dependence of the angular bandwidth, 2NA$_{\text{sub}}$, versus the FOV is easy to obtain from Fig. 3. The FOV (F) normalized to the slab thickness is

$$\frac{F}{t} = \tan \alpha_2 - \tan \alpha_1. \tag{12}$$

On the other hand, the marginal angles for a particular NA$_{\text{sub}}$ can be written as function of an angle $\sin \alpha_c$ of the center frequency, corresponding to the chosen HP$_c$:

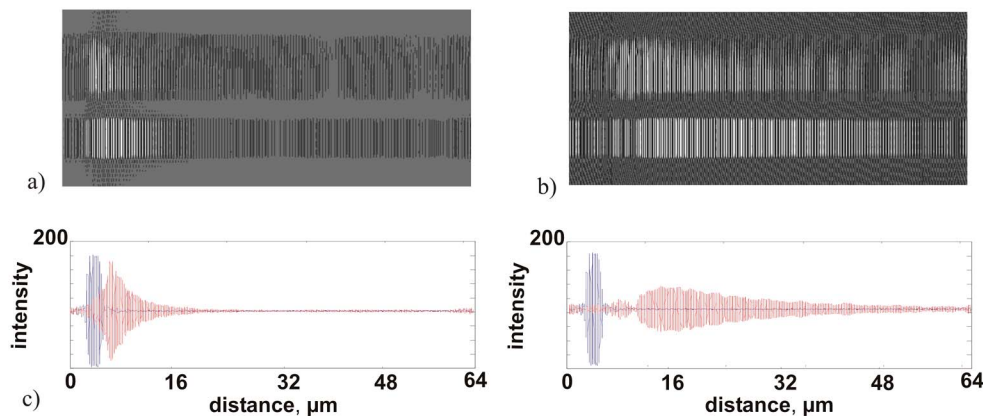$$\sin \alpha_2 = \sin \alpha_c + \text{NA}_{\text{sub}}, \tag{13}$$

Fig. 8. (Color online) Difference in expansion of spectral package (120 nm features) for different substrate thicknesses ($n = 1.5$, $F = 64$ μm): a) $t = 1$ μm, image expansion ~3 times; b) $t = 5$ μm, image expansion ~10 times; comparison of filtered image crosscuts (blue) with crosscuts of images (red) distorted by substrate propagation with: c) $t = 1$ μm, d) $t = 5$ μm.
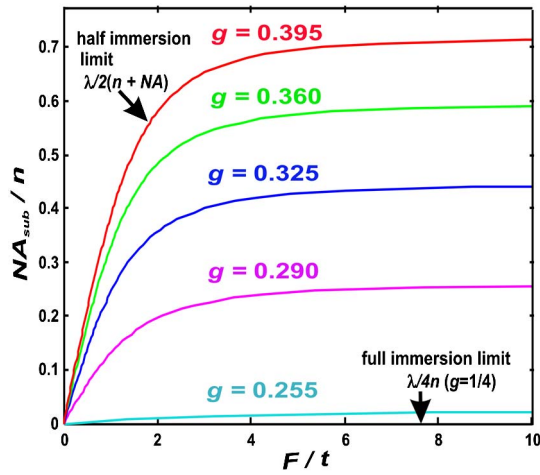
Fig. 9.   (Color online) Synthetic aperture guideline: normalized sub-image bandwidth 2NA$_{\text{sub}}$ versus normalized FOV for different extraction gratings represented by center frequency HP$_c$ ($g \equiv n\text{HP}_c/\lambda$).

$$\sin \alpha_1 = \sin \alpha_c - \text{NA}_{\text{sub}}, \tag{14}$$

where, for an illumination angle $\sin \beta$,

$$\sin \alpha_c + \sin \beta = \frac{\lambda}{2n\text{HP}_c}. \tag{15}$$

Combining Eqs. (12)–(14) gives an implicit relation for the optical system parameters

$$\frac{F}{t} = \frac{\sin \alpha_c + \frac{\text{NA}_{\text{sub}}}{n}}{\sqrt{1 - \left(\sin \alpha_c + \frac{\text{NA}_{\text{sub}}}{n}\right)^2}} - \frac{\sin \alpha_c - \frac{\text{NA}_{\text{sub}}}{n}}{\sqrt{1 - \left(\sin \alpha_c - \frac{\text{NA}_{\text{sub}}}{n}\right)^2}}. \tag{16}$$

This dependence, shown in Fig. 9 for several HP$_c$ normalized by n and λ ($g \equiv \frac{n\text{HP}_c}{\lambda}$), allows us to define the NA$_{\text{sub}}$ of each subimage and to estimate the number of subimages which are necessary to cover all of the available spatial frequency space (along a specific direction).

We can see from Fig. 9 that, in order to prevent the loss of information, we need an objective with a larger FOV or additional spatially shifted subimages to build a synthetic FOV. These conclusions are qualitatively the same as those drawn from Figs. 4 and 5.

Examples of images shown in Fig. 8 restored using a FOV of 16 μm are shown with corresponding crosscuts (red) in comparison with the undistorted image (green) and differences between the restored and filtered crosscuts in Fig. 10. Figure 10a) is obtained from Fig. 8a) and Fig. 10b) is obtained from Fig. 8b). It is clear that the subimage in Fig. 8a) for a 1 μm thick substrate is extended less than the subimage in Fig. 8b) for a 5 μm thick substrate, and the quality of the restored image in Fig. 10a) is higher than that in Fig. 10b). Extension of recorded FOV to 32 μm for the image in Fig. 8b) improves the quality of restored image [Fig. 10c)], showing the complex interrelationships between the resolution, FOV, NA, substrate thickness, and the refractive index.

For an additional perspective on the ability to restore these images, the restored images with different HP were compared with the filtered high-frequency images using a mean square error (MSE) metric. A simple 10-line grating pattern was chosen for MSE analyses (inside of the red square) and normalized to a gray field (Fig. 11). The curves of MSE versus HP for a $\lambda = 633$ nm, $n = 1.5$ substrate thicknesses of 0.5, 1, 3, 5, 10 μm and a restoration FOV of 32 μm are shown. For a comparable MSE procedure, it is important to have the spectral content of the image filtered similarly. Thus, we ensure that the center frequency at the HP always passes through the center of the collection objective, as in the derivation of Eq. (16).
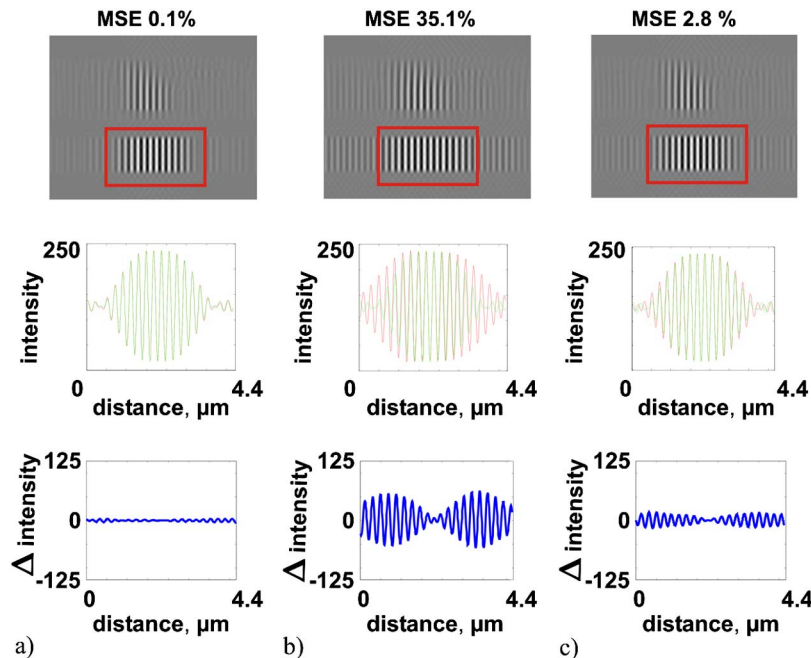

Fig. 10.   Restored images (CD = 120 nm, $n = 1.5$), crosscuts and crosscut differences: a) $t = 1$ μm, $F = 16$ μm—quality of the resorted image is good, b) $t = 5$ μm, $F = 16$ μm—quality of the resorted image is poor due to increased substrate thickness, c) $t = 5$ μm, $F = 32$ μm—quality of the resorted image is improved as the result of increasing FOV.
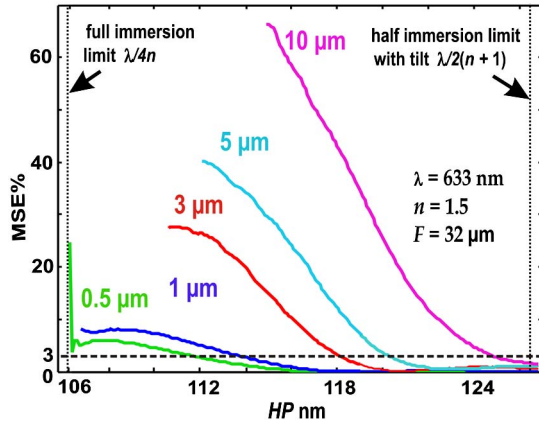
Fig. 11.   (Color online) MSE versus HP of a 10-line pattern for different substrate thicknesses, $n = 1.5$; $F = 32$ μm; $\lambda = 633$ nm. 3% MSE considered as images with acceptable quality. 0.5 μm substrates allows restoration of images with 112 nm features, 1 μm $\sim$ 113.5 nm, 3 μm $\sim$ 118 nm, 5 μm $\sim$ 120 nm, 10 μm $\sim$ 124 nm.

These calculations were carried out from the theoretical limit $\lambda/4n = 0.106$ μm to the half-immersion limit $\lambda/(n + 1) = 0.126$ μm ($\lambda = 633$ nm, $n = 1.5$). The MSE drops as the image becomes resolvable. As expected, the distortion (expansion of the frequency content across the detection plane) of image features is lower in thinner films, allowing higher resolution with a smaller FOV.

The same models were used for substrates with different refractive indices in order to evaluate possible resolvable HP with MSE = 3% for substrate thicknesses of 1, 5, and 10 μm. The results are summarized in Fig. 12, where the resolvable HP versus refractive index are shown. The lower black dashed curve $\lambda/4n$ is the theoretical limit of full-immersion resolution, and the black upper dashed line $\lambda/2(n + \text{NA})$ is the half-immersion limit with an untilted objective.

The modeling of image reconstruction represented in Fig. 12 qualitatively confirms the results obtained by investigation of theoretical resolution limit (Fig. 6). The image resolution depends on the optical system and substrate properties (NA, FOV, t, and n). The achievable resolution scales inversely with the substrate index of refraction. Substrate thicknesses greater than several times the FOV result in experimental
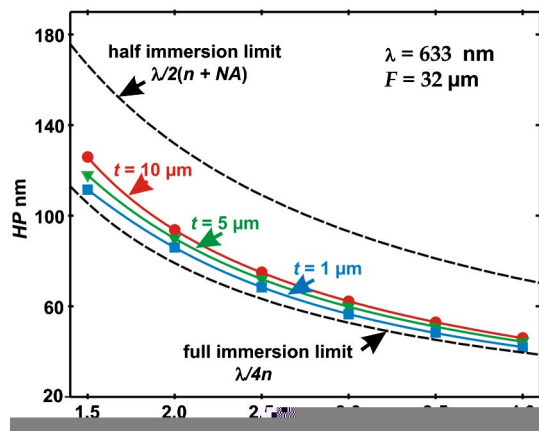

Fig. 12.   (Color online) HP versus n for different substrate thicknesses: 1, 5, 10 μm ($F = 32$ μm), $\lambda = 633$ nm. Substrates with higher n allow resolution and restoration of images with smaller features.

difficulties, both in registration and in lowered signal intensity, which can result in S/N issues.

4. CONCLUSIONS

The purpose of this paper is to show the advantages and limitations of IIN in a new configuration, where a slab of high-refractive-index material is used as an effective solid-immersion medium to enhance the resolution up to the linear-system resolution limit of $\lambda/4n$. Phase distortions of high-frequency subimages are inherent in the geometry of beam propagation in the immersion slab, requiring a phase restoration procedure. The resolution in this configuration depends not only on objective NA and FOV, but also on the captured portion of the spectral information, which is also a function of the immersion slab refractive index and thickness. The criteria for evaluation of the ultimate HP limits for different immersion slab parameters and system FOV have been provided. The estimation shows that the minimum thickness of the immersion slab and the maximum FOV of the optical system should be chosen to achieve the highest resolution with the smallest number of subimages.

These analyses also reveal a new regime for IIN. Using very thin substrates (or overlayers) and thereby restricting the propagation distance, higher absorption can be tolerated, allowing the use of shorter wavelengths. Then the resolution is improved by two factors—the shorter wavelength and the higher index of refraction within an absorption band. This approach provides resolutions that are not available to solid-immersion microscopy approaches as a result of the need for a thick (bulk material) high-index solid-immersion lens (SIL). Thin-layer structures, $t \sim \lambda/n$, present a more complex optical problem than the thick layers considered above, due to the need to include both interfaces in a single calculation with multiple scattering effects. However, in the presence of strong absorption, the multiple scattering effects are reduced and the single surface results are restored. A more detailed analysis is needed to elucidate the ultimate resolution limits as the substrate thickness is reduced relative to the absorption length and the wavelength.

Table 1 provides calculated resolutions for several microscopy techniques including annular illumination [47], SIL microscopy [48], along with IIN and compares the practical resolution available for different wavelengths with a silicon immersion substrate in the limit where separate single surface calculations are appropriate.

Annular illumination using the $\sim$2$\times$ resolution advantage of off-axis illumination can be combined with immersion techniques (current results are with liquid immersion and an NA = 1.3 [44]). However, this requires alignment between two specialized high-NA, small-FOV objectives, which is a challenging task. Even ignoring the fact that usually there is a trade-off between the FOV and the NA, such objectives cannot use materials with significant losses as a result of the required macroscopic optical thicknesses.

SILs provide a relatively cost-effective solution for increasing NA by a combination of standard objective with section of high index refraction sphere as solid-immersion media. This method has shown good resolution (to 145 nm using a Si SIL at 1.2 μm), but again it can only be used with relatively long wavelengths because the sphere section (which in practice is close to a hemisphere) requires essentially lossless

Table 1. Wavelength-Dependent Resolution on a Si Substrate for Different Techniques

Wavelength (nm)	1064	704	633	488	430
	Si properties				
Si refractive index	3.56	3.77	3.9	4.37	4.91
Si $1/e$ length (μm)	1070	6.5	3.5	0.98	0.31
Double pass transmission (0.5 μm)	0.99	0.86	0.74	0.36	0.04
	Alternative approaches				
Annular illumination (NA = 1.3) $\lambda/(4\,NA)$ [47]	205	135	122	94	83
SIL $\lambda/4n$ [48] (thick lens does not allow materials with loss)	75	—	—	—	—
	IIN				
$\lambda/4$ (no immersion)	266	176	158	122	108
$\lambda/[2(n+1)]$ (half-immersion)	115	74	65	45	36
$\lambda/4n$ (full-immersion)	75	47	41	28	22

Table 2. Examples of Possible Combinations of Materials and Wavelength for Enhanced Resolution

λ (nm)	λ (nm)	Immersion $\lambda/4n_{max}$
633	158	48 ($n = 3.3$, GaP)
		40 ($n = 4.0$, Si)
488	122	50 ($n = 2.45$, GaN)
		28 ($n = 4.37$, Si)
193	48	27 ($n = 1.8$, photoresist)
		23 ($n = 2.1$, garnet)
		19 ($n = 2.6$, Si_3N_4)

materials. To the contrary, IIN can provide up to few tens of nanometers' resolution with immersion media such as silicon at the visible (red to green) wavelengths while retaining the full FOV, large working distance, depth-of-field, and low cost of low-NA objectives.

Other materials coupled with wavelengths in proximity to a material bandgap in combination with our method can also provide excellent results. Some possible wavelength/material combinations to explore are shown in Table 2.

Thus, IIN can be very useful for imaging small features using a thin immersion slab with high n where the resolution approaches that of a SEM with a simple inexpensive technique that is applicable in a range of environments including air and water.

REFERENCES

1. E. Abbe, "Beiträge zur Theorie des Mikroskops und der mikroskopichen Wahrnehmung," Arch. Mikrosk. Anat. Entwichlungsmech **9**, 413–468 (1873).
2. F. Le, Clerc, M. Gross, and L. Collot, "Synthetic aperture experiment in the visible with on-axis digital heterodyne holography," Opt. Lett. **26**, 1550–1552 (2001).
3. J. H. Massig, "Digital off-axis holography with a synthetic aperture," Opt. Lett. **27**, 2179–2181 (2002).
4. Z. Zalevsky and D. Mendlovic, *Optical Super Resolution* (Springer, 2002).
5. Z. Zalevsky, D. Mendlovic, and A. W. Lohmann, "Optical systems with improved resolving power," in *Progress in Optics*, Vol. 15, E. Wolf, ed. (1999), Chap. 4.
6. G. Toraldo di Francia, "Resolving power and information," J. Opt. Soc. Am. **45**, 497–501 (1955).
7. G. Toraldo di Francia, "Degrees of freedom of an image," J. Opt. Soc. Am. **59**, 799–804 (1969).
8. I. J. Cox and J. R. Sheppard, "Information capacity and resolution in an optical system," J. Opt. Soc. Am. A **3**, 1152–1158 (1986).
9. W. Lukosz, "Optical systems with resolving powers exceeding the classical limit. II," J. Opt. Soc. Am. **57**, 932–941 (1967).
10. A. Shemer, D. Mendlovic, Z. Zalevsky, J. Garcia, and P. García-Martínez, "Superresolving optical system with time multiplexing and computer decoding," Appl. Opt. **38**, 7245–7251 (1999).
11. P. C. Sun and E. N. Leith, "Superresolution by spatial-temporal encoding methods," Appl. Opt. **31**, 4857–4862 (1992).
12. M. Françon, "Amélioration de la reśolution d'optique," Nuovo Cimento Suppl. **9**, 283–287 (1952).
13. A. W. Lohmann and D. P. Parish, "Superresolution for nonbirefringent objects," Appl. Opt. **3**, 1037–1043 (1964).
14. A. Zlotnik, Z. Zalevsky, and E. Marom, "Superresolution with nonorthogonal polarization coding," Appl. Opt. **44**, 3705–3715 (2005).
15. A. I. Kartashev, "Optical system with enhanced resolving power," Opt. Spectrosc. **9**, 204–206 (1960).
16. S. A. Alexandrov, T. R. Hillman, and D. D. Sampson, "Spatially resolved Fourier holographic light scattering angular spectroscopy," Opt. Lett. **30**, 3305–3307 (2005).
17. S. A. Alexandrov, T. R. Hillman, T. Gutzler, and D. D. Sampson, "Synthetic aperture Fourier holographic optical microscopy," Phys. Rev. Lett. **97**, 168102 (2006).
18. S. A. Alexandrov, T. R. Hillman, T. Gutzler, and D. D. Sampson, "Digital Fourier holography enables wide-field, superresolved, microscopic characterization," Opt. Photon. News **18**, 29 (2007).
19. S. A. Alexandrov and D. D. Sampson, "Spatial information transmission beyond a systems diffraction limit using optical spectral encoding of the spatial frequency," J. Opt. A. **10**, 025304 (2008).
20. V. Mico, Z. Zalevsky, P. Garcia-Martinez, and J. Garcia, "Single-step superresolution by interferometric imaging," Opt. Express **12**, 2589–2595 (2004).
21. V. Mico, Z. Zalevsky, P. Garcia-Martinez, and J. Garcia, "Super-resolved imaging in digital holography by superposition of tilted wavefronts," Appl. Opt. **45**, 822–826 (2006).
22. V. Mico, Z. Zalevsky, and J. Garcia, "Superresolution optical system by common-path interferometry," Opt. Express **14**, 5168–5177 (2006).
23. E. N. Leith, D. Angell, and C.-P. Kuei, "Superresolution by incoherent-to-coherent conversion," J. Opt. Soc. Am. A **4**, 1050–1054 (1987).
24. E. N. Leith, "Small-aperture, high-resolution, two-channel imaging system," Opt. Lett. **15**, 885–887 (1990).
25. V. Mico, Z. Zalevsky, P. García-Martínez, and J. García, "Synthetic aperture superresolution with multiple off-axis holograms," J. Opt. Soc. Am. A **23**, 3162–3170 (2006).
26. C. J. R. Sheppard and Z. Hegedus, "Resolution for off-axis illumination," J. Opt. Soc. Am. A **15**, 622–624 (1998).
27. V. Mico, Z. Zalevsky, and J. García, "Common-path phase-shifting digital holographic microscopy: a way to quantitative imaging and superresolution," Opt. Commun. **281**, 4273–4281 (2008).
28. L. Granero, V. Micó, Z. Zalevsky, and J. García, "Superresolution imaging method using phase-shifting digital lensless Fourier holography," Opt. Express **17**, 15008–15022 (2009).
29. V. Micó, J. García, and Z. Zalevsky, "Axial superresolution by synthetic aperture generation," J. Opt. A. **10**, 125001 (2008).
30. V. Mico, Z. Zalevsky, C. Ferreira, and J. García, "Superresolution digital holographic microscopy for three-dimensional samples," Opt. Express **16**, 19260–19270 (2008).
31. S. Tyler, D. L. Ralston, P. Marks, S. Carney, and S. A. Boppart, "Interferometric synthetic aperture microscopy," Nat. Phys. **3**, 129–134 (2007).
32. S. Tyler, D. L. Ralston, P. Marks, S. Carney, and S. A. Boppart, "Real-time interferometric synthetic aperture microscopy," Opt. Express **16**, 2555–2569 (2008).
33. B. J. Davis, D. L. Marks, T. S. Ralston, P. S. Carney, and S. A. Boppart, "Interferometric synthetic aperture microscopy: computed imaging for scanned coherent microscopy," Sensors **8**, 3903–3931 (2008).

34. V. Lauer, "New approach to optical diffraction tomography yielding a vector equation of diffraction tomography and a novel tomographic microscope," J. Microsc. **205**, 165–176 (2002).

35. A. Sentenac, P. C. Chaumet, and K. Belkebir, "Beyond the Rayleigh criterion: grating assisted far-field optical diffraction tomography," Phys. Rev. Lett. **97**, 243901 (2006).

36. G. Maire, F. Drsek, J. Girard, H. Giovannini, A. Talneau, D. Konan, K. Belkebir, P. C. Chaumet, and A. Sentenac, "Experimental demonstration of quantitative imaging beyond Abbe's limit with optical diffraction tomography," Phys. Rev. Lett. **102**, 213905 (2009).

37. S. W. Hell, "Far-field optical nanoscopy (review)," Science **316**, 1153–1158 (2007).

38. Z. Jacob, L. V. Alekseyev, and E. Narimanov, "Optical hyperlens: far-field imaging beyond the diffraction limit," Opt. Express **14**, 8247–8256 (2006).

39. Z. Liu, H. Lee, Y. Xiong, C. Sun, and X. Zhang, "Far-field optical hyperlens magnifying sub-diffraction-limited objects," Science **315**, 1686 (2007).

40. C. J. Schwarz, Y. Kuznetsova, and S. R. J. Brueck, "Imaging interferometric microscopy," Opt. Lett. **28**, 1424–1426 (2003).

41. Y. Kuznetsova, A. Neumann, and S. R. J. Brueck, "Imaging interferometric microscopy—approaching the linear systems limits of optical resolution," Opt. Express **15**, 6651–6663 (2007).

42. Y. Kuznetsova, A. Neumann, and S. R. J. Brueck, "Imaging interferometric microscopy," J. Opt. Soc. Am. A **25**, 811–822 (2008).

43. A. Neumann, Y. Kusnetsova, and S. R. J. Brueck, "Structured illumination for the extension of imaging interferometric lithography," Opt. Express **16**, 6785–6793 (2008).

44. A. Vainrub, O. Pustovyy, and V. Vodyanoy, "Resolution of 90 nm ($\lambda/5$) in an optical transmission microscope with annular condenser," Opt. Lett. **31**, 2855–2857 (2006).

45. F. H. Koklu, S. B. Ippolito, B. B. Goldberg, and M. S. Unlu, "Subsurface microscopy of integrated circuits with angular spectrum and polarization control," Opt. Lett. **34**, 1261–1263 (2009).

46. A. Neumann, Y. Kuznetsova, and S. R. J. Brueck, "Optical resolution below $\lambda/4$ using synthetic aperture microscopy and evanescent-wave illumination," Opt. Express **16**, 20477–20485 (2008).

47. A. Vainrub, O. Pustovyy, and V. Vodyanoy, "Resolution of 90 nm ($\lambda/5$) in an optical transmission microscope with an annular condenser," Opt. Lett. **31**, 2855–2857 (2006).

48. F. H. Koklu, S. B. Ippolito, B. B. Goldberg, and M. S. Unlu, "Subsurface microscopy of integrated circuits with angular spectrum and polarization control," Opt. Lett. **34**, 1261–1263 (2009).